Journal of Materials Chemistry A

COMMUNICATION

View Article Online
View Journal | View Issue

Cite this: *J. Mater. Chem. A*, 2019, **7**, 26279

Received 27th September 2019
Accepted 4th November 2019

DOI: 10.1039/c9ta10704e

rsc.li/materials-a

Unveiling the role of tetragonal $BiVO_4$ as a mediator for dual phase $BiVO_4$/g-C_3N_4 composite photocatalysts enabling highly efficient water oxidation *via* *Z*-scheme charge transfer†

Hyung Jun Kong,‡[a] Keon-Han Kim,‡[a] Sangjun Kim,[a] Heebin Lee[b] and Jeung Ku Kang *[ab]

Monoclinic scheelite $BiVO_4$ (BVO-M) based materials are of great interest as photocatalysts for water oxidation essential to produce value-added chemical fuels, but their slow charge transfer and low activity are yet to be resolved. As a solution to overcome this challenge, we report *Z*-scheme photocatalyst fabricated by integrating the dual phase structure of monoclinic scheelite and tetragonal zircon-type $BiVO_4$ (BVO-T) moieties with graphitic carbon nitride (g-C_3N_4) having π-conjugated two dimensional layers suited to visible light-induced charge transfer. Moreover, V K-edge and Bi L3-edge X-ray absorption near-edge structure (XANES) and Fourier transformed extended X-ray absorption fine structure (EXAFS) spectra demonstrate that the tetragonal zircon-type $BiVO_4$ structures in a *Z*-scheme catalyst form a bridge between BVO-M and g-C_3N_4 structures so that it acts as an electron mediator to accelerate charge transfer, in agreement with the zeta-potential analysis and the band structure revealed by UV-vis spectroscopy and ultraviolet photoelectron spectroscopy analyses. Furthermore, a *Z*-scheme photocatalyst is exhibited to show a 3-fold longer charge carrier lifetime than BVO-M, thereby enabling the greater than three-fold enhancement in photocatalytic water oxidation activity. Additionally, isotope ^{18}O-labelling experiments reveal that evolved oxygen molecules result from water through photocatalytic water oxidation.

The global energy consumption is primarily based on fossil fuels, but their combustion to generate electricity creates oxidized molecules such as carbon dioxide, sulphur oxide, and nitrous oxide leading to pollution and climate change.[1–3] On the other hand, artificial photosynthesis consisting of two key steps, where the first step is water oxidation to generate protons and electrons from water using solar energy, and the second one is to convert oxidized molecules into useful chemical fuels using their isolated protons and electrons, is an appealing method to produce value-added chemical fuels.[4,5] Achieving efficient photocatalytic water oxidation is challenging because the formation of oxygen from water requires transfer of 4 holes.

BVO-M is one of the most promising materials in that it allows visible light-induced water oxidation with an appropriate bandgap (2.4 eV) for absorbing visible light and a good valence-band edge placement necessary to oxidize water with photoexcited holes.[6–9] Typically, $BiVO_4$ is known to have three different crystal forms including monoclinic scheelite, tetragonal scheelite, and tetragonal zircon-type structures. Especially, the monoclinic scheelite crystal structure exhibits greater solar photocatalytic activity than the other types of structures because the valence band molecular orbitals are hybridized with Bi 6s and O 2p atomic orbitals to have the reduced bandgap that can absorb visible light,[10] while the tetragonal $BiVO_4$ having a larger bandgap (2.9 eV) can barely respond to visible light.[11] Moreover, the lone-pair distortion in BVO-M could promote hole migration.[12] Despite these advantages, the challenge exists in that BVO-M suffers from slow charge transfer rates attributed to the fast recombination of photoexcited charge carriers (*i.e.* excitons). These characteristic properties support that providing a new hierarchical complex or methodology enabling fast charge transfer would provide a novel route to enable high activity in photocatalytic water oxidation.[13]

Herein, we show a *Z*-scheme charge transfer photocatalyst integrated using dual-phase $BiVO_4$ and g-C_3N_4, where the impregnated co-precipitation method was utilized to realize a *Z*-scheme photocatalyst using the co-existing monoclinic and tetragonal dual-phase $BiVO_4$ structure in conjunction with g-C_3N_4 having π-conjugated two-dimensional layers well suited to visible light-induced charge transfer (Fig. 1a). Also, the scanning electron microscopy (SEM) images elucidate the morphological difference between monoclinic and tetragonal $BiVO_4$ phases. BVO-M has a well-crystalized morphology with 200–300 nm crystals (Fig. S1a†). By contrast, tetragonal $BiVO_4$ (BVO-

[a]*Department of Materials Science and Engineering, Korea Advanced Institute of Science and Technology, 291 Daehak-ro, Yuseong-gu, Daejeon 34141, Republic of Korea. E-mail: jeungku@kaist.ac.kr*

[b]*Graduate School of EEWS, Korea Advanced Institute of Science and Technology, 291 Daehak-ro, Yuseong-gu, Daejeon 34141, Republic of Korea*

† Electronic supplementary information (ESI) available. See DOI: 10.1039/c9ta10704e

‡ H. J. Kong and K.-H. Kim contributed equally to this work.

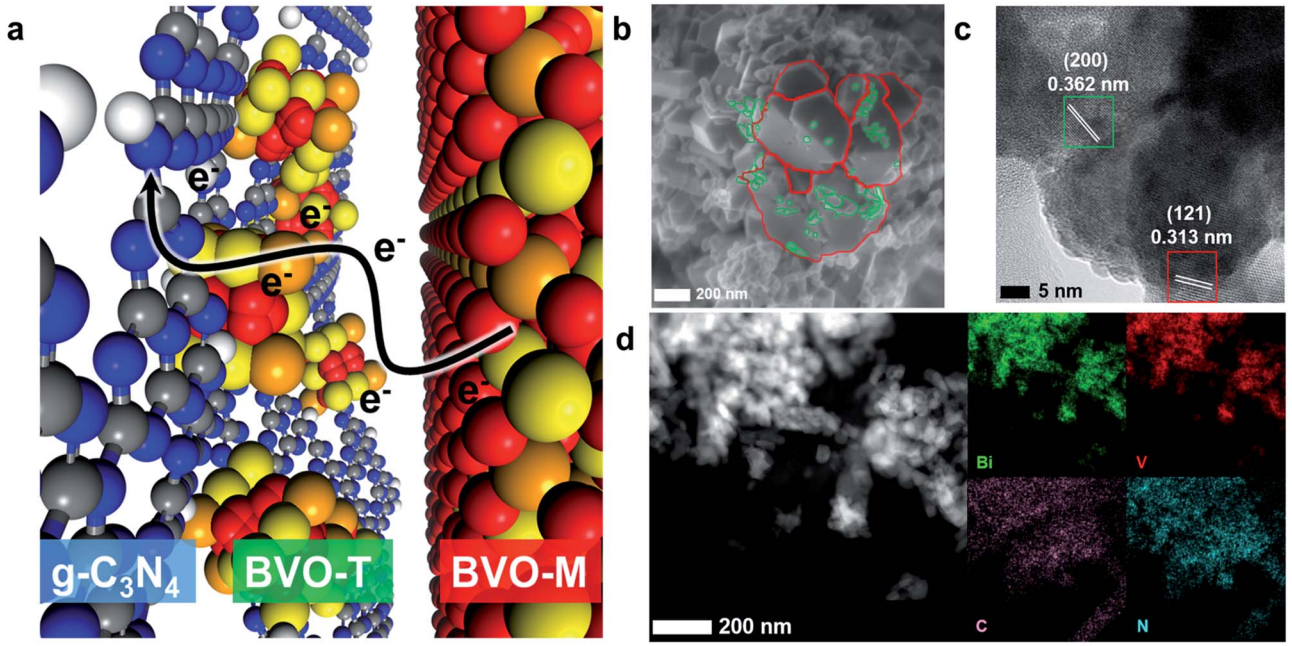

Fig. 1 (a) The schematic illustration of a dual-phase $BiVO_4$/g-C_3N_4 composite photocatalyst for water oxidation. (b) The SEM image of BVO-D (red: BVO-M; green: BVO-T). (c) The TEM image of BC-D. (d) The EDS mapping of BC-D.

T) has 20–100 nm spherical crystals (Fig. S1b†). However, dual-phase $BiVO_4$ (BVO-D) exhibits a mixed morphology of BVO-M and BVO-T (Fig. 1b). Fig. S1c and d† clarify that the composite photocatalyst fabricated using monoclinic $BiVO_4$ (BC-M) shows a (121) plane having 0.313 nm lattice spacing. Similarly, the composite photocatalyst fabricated using tetragonal $BiVO_4$ (BC-T) has a (200) plane with 0.362 nm lattice spacing.[14] Additionally, the transmission electroscope microscopy (TEM) image (Fig. 1c) clarifies that both monoclinic and tetragonal crystal phases co-exist in a dual-phase $BiVO_4$/g-C_3N_4 composite photocatalyst (BC-D). Scanning transmission electron microscopy with energy-dispersive spectrometry (STEM-EDS) mapping shows that the crystal structure contains bismuth and vanadium elements for $BiVO_4$, along with carbon and nitrogen elements for g-C_3N_4 (Fig. 1d and S2†).

Also, the crystal structures of all the samples were verified through X-ray diffraction (XRD) analysis. Fig. S3† shows the XRD patterns for BVO-M and BVO-T. The main peak of BVO-M appears at 28.9° representing the (121) plane, whereas the characteristic peak of BVO-T appears at 24.3° attributed to the (200) plane.[15] In addition, we find that the XRD peaks for BVO-M agree with those in card no. 14-0688 of the Joint Committee on Powder Diffraction Standards (JCPDS). Meanwhile, BVO-D has the main XRD peaks corresponding to both of the monoclinic and tetragonal crystal structures. For the composite photocatalysts, a very small and broad XRD peak at 27° is attributed to g-C_3N_4 (Fig. S4†). Fig. 2a indicates that the XRD pattern of $BiVO_4$ is unchanged after the composite is formed. By contrast, BC-T shows a dramatic decrease in peak intensity compared with that of BVO-T, attributed to the increased proportion of g-C_3N_4 in the composite catalyst. Furthermore, the ratios of $BiVO_4$ and g-C_3N_4 in the composite catalyst were quantified through thermogravimetric analysis (Fig. S5†). $BiVO_4$ and g-C_3N_4 have different melting points. At temperatures greater than 550 °C, most of the g-C_3N_4 was determined to be decomposed. Each composite photocatalyst contains a different amount of $BiVO_4$. BC-T contained 50% $BiVO_4$, whereas BC-M contained 80% $BiVO_4$. This indicates that tetragonal $BiVO_4$ is superior to monoclinic $BiVO_4$ for the formation of a composite with g-C_3N_4. In addition, we observe the Raman spectral peaks (Fig. 2b) at 473 cm^{-1}, 707 cm^{-1} and 1234 cm^{-1} appearing for the samples containing g-C_3N_4.[16,17] BC-M and BC-D show identical peaks

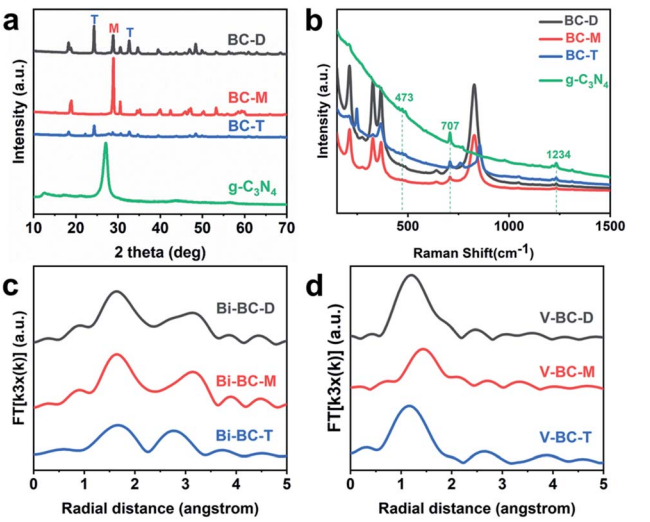

Fig. 2 (a) The XRD patterns, (b) the Raman spectra, and (c and d) the EXAFS spectra of the composite photocatalysts (c: bismuth; d: vanadium).

attributed to VO_4 tetrahedrons. The intensity ratios of the peaks at 367 cm^{-1} and 327 cm^{-1} in the Raman spectra, which represent the symmetric bending mode and antisymmetric bending mode of V–O bonds, respectively, were also determined to be similar. However, BC-T showed different stretching and bending modes of the VO_4 tetrahedron. This indicates that the dual-phase $BiVO_4$ is mainly composed of the VO_4 tetrahedral monoclinic $BiVO_4$ phase. Moreover, the local atomic structures were explored through X-ray absorption spectroscopy (XAS) measurements on Bi and V elements. Fig. S6a† shows the XANES spectra at the Bi L3-edge of the composite catalysts. The sharp edge peaks at 13 430 eV are attributed to the dipole-allowed $2p_{3/2}$–6d transition,[18] indicating that bismuth is in the Bi^{3+} oxidation state. Moreover, $BiVO_4$ samples without g-C_3N_4 show the same XANES spectra (Fig. S7a†), supporting that Bi is in the Bi^{3+} state.[19] Furthermore, the Fourier transformed EXAFS spectra elucidate the radial distance of Bi ions in coordination with the surrounding atoms. The radial distance of Bi–O bonds for BVO-M, BVO-T and BVO-D (Fig. S7b†) is 1.76 Å. However, the Bi-metal bonding centred at the second peak is found to differ for BVO-M (2.76 Å) and BVO-T (3.09 Å). Moreover, the spectra of BVO-D show the two aforementioned peaks. Fig. 2c also shows the EXAFS spectra of the composite photocatalysts. The first shell centred at 1.64 Å was decreased after composite formation with g-C_3N_4. The two peaks formed at the second shell indicate that the Bi–O bond length is the same as that in $BiVO_4$ without g-C_3N_4. Additionally, the V K-edge XANES and EXAFS spectra (Fig. 2d and S6b†) show the same trends as those for the Bi spectra, indicating that V ions are in the same oxidation state in the composite. Therefore, these XAS spectra exhibit clearly the local atomic configurations for the synthesized monoclinic–tetragonal dual phases and monoclinic–tetragonal–g-C_3N_4 composites.

To verify the bond between $BiVO_4$ and g-C_3N_4, X-ray photoelectron spectroscopy (XPS) measurements were also performed. For the synthesis of composite photocatalysts, g-C_3N_4 was impregnated in the precursor solution (2 M nitric acid). During this impregnation, the surface of g-C_3N_4 is oxidized and VO_4^{3-} is formed on the surface. Accordingly, the oxygen-related peaks in the C 1s and N 1s spectra indicate the formation of a $BiVO_4$/g-C_3N_4 composite. Furthermore, deconvolution demonstrates that the oxygen-related peaks exist in the C 1s and N 1s XPS spectra of BC-D. The peak at 286.23 eV (Fig. 3a) is associated with hydroxyl groups attached to the carbon nitride surface, while the peak at 406.53 eV (Fig. 3b) supports the presence of nitrate groups generated during impregnation. The areas of these peaks were determined to be larger than those of BC-M and BC-T (Fig. S8†), indicating that the dual phase $BiVO_4$ is better to realize a *Z*-scheme composite photocatalyst in conjunction with g-C_3N_4. Also, the zeta potentials of the photocatalysts (Fig. 3c) were measured to elucidate the principle of composite catalyst formation. The zeta potential of BVO-M was −53 mV and that of BVO-T was +50 mV. It is notable that the difference in these zeta potentials is attributed to different surface charges. The surface charge is also found to affect the composite formation. g-C_3N_4 has a negative surface charge in the solution where positively charged particles can combine,

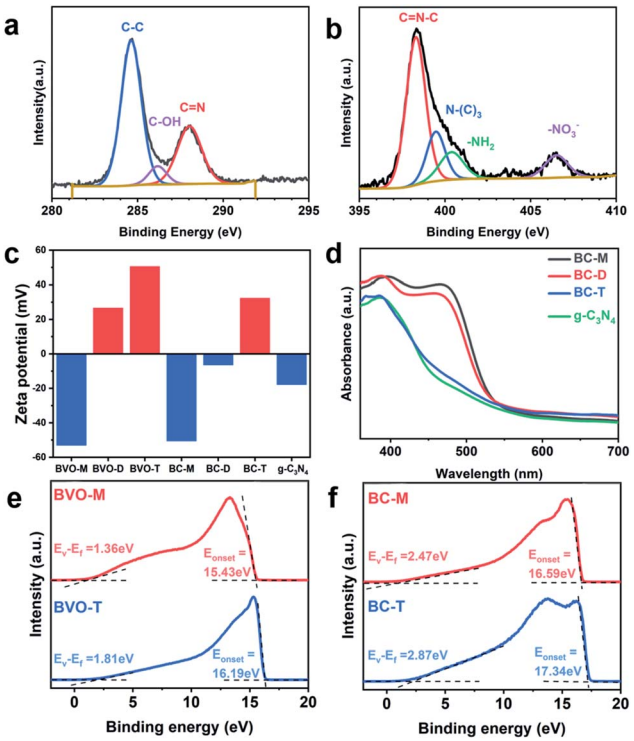

Fig. 3 (a and b) The XPS spectra of BC-D (a: C 1s; b: N 1s). (c) The zeta potential of the prepared photocatalyst. (d) The UV-vis spectra of the prepared photocatalysts and g-C_3N_4. (e and f) The UPS spectra of the prepared photocatalysts.

while both BVO-T and BVO-D exhibit positive zeta potentials. This supports that the coulombic attraction exists between BVO-T and g-C_3N_4 structures. Also, zeta potentials support that the composition of dual phase $BiVO_4$ and g-C_3N_4 structures is spontaneous. Additionally, the band structures were determined through ultraviolet-visible spectroscopy (UV-vis) and ultraviolet photoelectron spectroscopy (UPS) analyses. The Tauc plots indicate that the bandgap energy of BVO-T is 2.88 eV, whereas that of BVO-M is 2.45 eV (Fig. S9†). In the spectra of BVO-D, the tail of the peak is observed to be located at 550 nm similar to the position of the absorbance peak tail of BVO-M. However, BVO-D exhibits the optical bandgaps of both BVO-M and BVO-T. The composite photocatalysts exhibit a change in absorption of visible light (Fig. 3d). It is notable that the absorbance spectrum of BC-T is very similar to that of g-C_3N_4. The band structure could be obtained with the values of the optical bandgap, work-function, and energy position value of the valence-band maximum (E_v) from the UPS spectra (Fig. 3e and f). First, we calculated the work function by subtracting E_{onset} from the incident photon energy using the following equation of

$$\text{Work function} = h\nu - E_{onset} \quad (1)$$

where $h\nu$ is a fixed value of 21.2 eV and E_{onset} is determined by the linear extrapolation of the secondary electron emission peaks.[18] E_v can be obtained from the intersection point between

the baseline and the linear extrapolation line from initial onset position around the Fermi level (E_f). We summarized the band structure energy levels in Table S1.†

From E_c, E_v and E_f values calculated from Fig. 3e, we identified that the band structure of BVO-M has the energy levels of −7.13 and −4.69 eV (*versus* vacuum) for E_v and E_c, respectively, consistent with previous results.[20,21] BVO-T has the values of −6.82 and −4.19 eV (*versus* vacuum) for E_v and E_c, respectively. In addition, Fig. S10† reveals that the E_v and E_c values of g-C_3N_4 are −6.26 and −3.66 eV (*versus* vacuum). Moreover, composite photocatalysts composed of these three materials are found to have the band structures suitable for *Z*-scheme charge transfer (Scheme S1†).

In order to determine the junctions throughout the component of composite materials, we have also analysed UPS spectra of BC-M and BC-T (Fig. 3f). After chemical bonding with g-C_3N_4, BC-M is determined to have p-type semiconductor properties because the Fermi level value of BC-M is located at the lower position than E_i. To probe the conducting properties of BC-M under experimental conditions, Mott–Schottky analysis was carried out and the results in Fig. S11† clarify that BC-M has a negative slope in the Mott–Schottky plot. This indicates that BC-M has p-type semiconductor properties, which is well matched with UPS data. Meanwhile, the tetragonal $BiVO_4$ based materials containing BVO-T and BC-T are maintained with an n-type nature. Since BC-D forms a composite with BC-M and tetragonal based materials, p–n junctions throughout the components of BC-D are formed. This result supports that a space charge region is generated by a p–n junction near the depletion region which electrons in n-type tetragonal $BiVO_4$ based materials and holes in p-type BC-M are depleted. It is notable that electric fields are generated in the space charge region facilitating the transfer of majority carriers, thereby helping to promote photocatalytic water oxidation activity in the case of BC-D. Therefore, the surface charge difference and surface oxidation of g-C_3N_4 provide an environment for composite photocatalyst formation, where *Z*-scheme and p–n junctions suppress charge recombination thus leading to efficient photocatalytic water oxidation.

Furthermore, we explored the activity for photocatalytic water oxidation through gas chromatography (Fig. 4a). Photocatalytic activity was determined at an optimal ratio of 1 g L^{-1} for catalyst concentration to give a precise quantitative comparison (Fig. S12†).[22] The oxygen evolution rate of BVO-M is determined to be the highest among pristine $BiVO_4$ because of its narrowest bandgap energy and lone-pair distortion. Meanwhile, BVO-D gives moderate water oxidation performance, whereas BVO-T hardly oxidizes water. However, the composite photocatalysts exhibited different photocatalytic activity trends. BC-D exhibited the highest catalytic activity—even higher than that of BVO-M. The oxygen evolution rate of BC-T slightly increased compared with that of pristine BVO-T. On the other hand, the oxygen evolution rate of BC-M decreased compared with that of pristine BVO-M. The composite catalyst has a *Z*-scheme electron pathway advantageous for inhibiting charge recombination. High performance in photocatalytic water oxidation requires the consumption of photoexcited electrons.

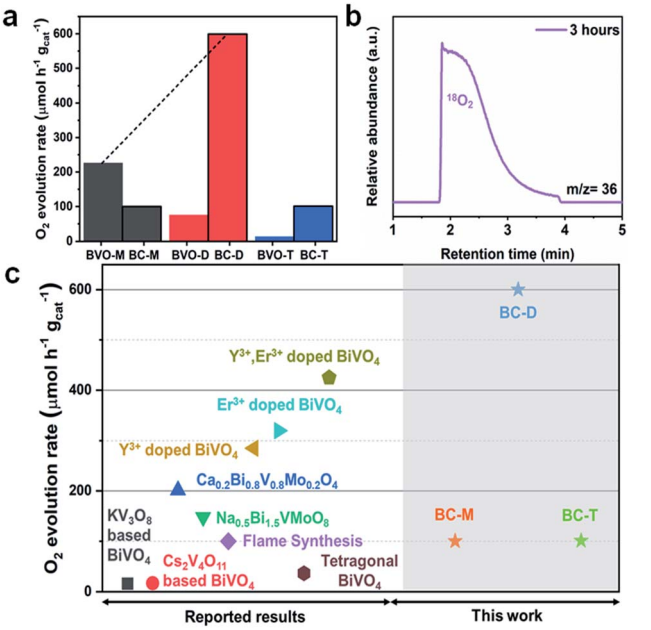

Fig. 4 (a) The oxygen evolution rates of the prepared photocatalysts. (b) The mass spectrum of evolved oxygen from the isotope $H_2{}^{18}O$. (c) The comparison of the oxygen evolution rates of the prepared photocatalysts with those of other previous $BiVO_4$ photocatalysts reported in the literature.

As evident in the aforementioned characterization, tetragonal $BiVO_4$ is more favourable for composite formation with g-C_3N_4, but it shows negligible photocatalytic activity. BC-D shows both high photocatalytic activity and also the ability to form a composite with g-C_3N_4. Also, BC-D gives not only a remarkably high oxygen evolution rate of about 600 μmol h^{-1} g^{-1}, but also an excellent external quantum efficiency of 2.36% under AM1.5G illumination conditions. Furthermore, to verify that the evolved oxygen was generated *via* photocatalytic reaction, $H_2{}^{18}O$ mass spectroscopic detection experiments were carried out with gas chromatography analysis, where a 0.05 M $Ag(NO)_3$ solution prepared with 1 mL of $H_2{}^{18}O$ was added to 9 mL of $H_2{}^{16}O$ and the resulting mixture was used in isotope tracer experiments on 10 mg of BC-D photocatalysts. Fig. 4b shows a peak at $m/z = 36$ assigned to $^{18}O_2$, indicating that $H_2{}^{18}O$ was oxidized to $^{18}O_2$ through photocatalytic water oxidation. Also, the lifetime of charge carriers (τ_1) was measured through time-correlated single-photon counting (TCSPC) analysis. BVO-M showed a τ_1 of 1.38 ns, supporting that the charge carriers did not exist long enough to react with water. The charge-carrier lifetime of BVO-T was longer than that of BVO-M, but it was still shorter than 2 ns. After composite formation, the lifetime was determined to be increased. Table S2† clarifies that BC-D and BC-T have lifetimes longer than 4 ns. The composite photocatalysts with g-C_3N_4 enable *Z*-scheme charge transfer, so that their charge recombination rates could be effectively reduced. *Z*-scheme charge transfer can be verified by PL analysis. The PL peak of pristine $BiVO_4$ is located at 620 nm (ref. 23) (Fig. S13a†) and that of g-C_3N_4 has the PL peak at 450 nm.[24] However, the composite photocatalysts show a different PL peak located from 500 to 550

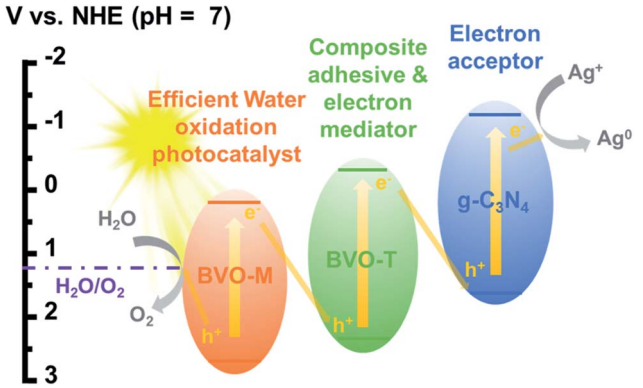

Fig. 5 The proposed mechanism for photocatalytic water oxidation through a monoclinic–tetragonal dual-phase $BiVO_4$/g-C_3N_4 composite photocatalyst.

nm, which is an indication for *Z*-scheme charge transfer because the inter-particle charge transfer derived peak is not matched with the PL peak of either $BiVO_4$ or g-C_3N_4.[25] Furthermore, the PL intensity of BC-D is shown to be smaller than that of BC-M and BC-T, verifying that BC-D shows the highest efficiency for charge separation (Fig. S13b†). Moreover, Fig. 4c shows a comparison chart of oxygen evolution rates in this work and previous reports.[10,26–31] These results imply that high performance in photocatalytic water oxidation could be achieved on a novel structure enabling *Z*-scheme charge transfer, as demonstrated in our composite photocatalysts fabricated using monoclinic–tetragonal dual phase $BiVO_4$ and g-C_3N_4 structures.

Fig. 5 also summarizes the water oxidation mechanism for BC-D composed of BVO-M, BVO-T and g-C_3N_4 whose band structures enable *Z*-scheme charge transfer. Meanwhile, charge transfer in the composite photocatalyst is determined by not only the band structure, but also by which reaction prevails in each composite component. It is notable that $BiVO_4$ has superior water oxidation catalytic properties and g-C_3N_4 provides various reduction catalyst sites. Although g-C_3N_4 could show a water oxidation catalyst property as a single component catalyst, the results (Fig. S14†) demonstrate that it shows a lower activity than $BiVO_4$. Therefore, in the case where g-C_3N_4 forms a composite with $BiVO_4$, water oxidation occurs in $BiVO_4$ and the remaining electrons move toward g-C_3N_4 to reduce Ag ions to Ag as described in Fig. 5.

In conclusion, we discovered that tetragonal $BiVO_4$ in this *Z*-scheme charge transfer catalyst acts as an adhesive bridge between BVO-M and g-C_3N_4, so that charge transfer between the dual-phase $BiVO_4$ and g-C_3N_4 can be accelerated through the oxygen atoms of VO_4 tetrahedrons and g-C_3N_4 structures, thereby enabling high photocatalytic water oxidation activity.

Conclusions

A dual phase $BiVO_4$ material comprising monoclinic scheelite and tetragonal zircon-type structures was successfully synthesized and its advantage in forming a *Z*-scheme composite photocatalyst with g-C_3N_4 was demonstrated. The coulombic attraction originating from differences in their surface charges and surface oxidation states led to the formation of composite photocatalysts. In addition, we found that the positive zeta potential of tetragonal zircon-type $BiVO_4$ is a driving force to bridge with monoclinic $BiVO_4$ and g-C_3N_4 structures. Moreover, the composite photocatalyst was exhibited to give an about 3-fold longer charge carrier lifetime than pristine $BiVO_4$, which in turn resulted in a greater than three-fold enhancement in photocatalytic water oxidation activity. Furthermore, isotope ^{18}O-labelling experiments proved that evolved oxygen molecules resulted from water. This demonstrates the great promise of tetragonal $BiVO_4$ in forming *Z*-scheme composites with monoclinic $BiVO_4$ for high performance in photocatalytic water oxidation. Consequently, we anticipate that this work would provide new insights into the design of high-performance photocatalysts allowing fast charge transfer, thereby enabling high activity in water oxidation.

Conflicts of interest

There are no conflicts to declare.

Acknowledgements

H. J. Kong and K.-H. Kim contributed equally to this work. This research was mainly supported by the Global Frontier R&D Program of the Center for Hybrid Interface Materials (2013M3A6B1078884) and the Korea Center for Artificial Photosynthesis (2009-0093881) funded by the Ministry of Science, ICT & Future Planning, and the National Research Foundation of Korea (2017M2A2A6A01070673 and 2019M3E6A1066150).

References

1 M. Meinshausen, N. Meinshausen, W. Hare, S. C. B. Raper, K. Frieler, R. Knutti, D. J. Frame and M. R. Allen, *Nature*, 2009, **458**, 1158.
2 G. P. Peters, R. M. Andrew, T. Boden, J. G. Canadell, P. Ciais, C. Le Quéré, G. Marland, M. R. Raupach and C. Wilson, *Nat. Clim. Change*, 2012, **3**, 4.
3 H. D. Matthews, N. P. Gillett, P. A. Stott and K. Zickfeld, *Nature*, 2009, **459**, 829–832.
4 D. Gust, T. A. Moore and A. L. Moore, *Acc. Chem. Res.*, 2009, **42**, 1890–1898.
5 D. Kim, K. K. Sakimoto, D. Hong and P. Yang, *Angew. Chem., Int. Ed.*, 2015, **54**, 3259–3266.
6 Y. Park, K. J. McDonald and K.-S. Choi, *Chem. Soc. Rev.*, 2013, **42**, 2321–2337.
7 A. Kudo and Y. Miseki, *Chem. Soc. Rev.*, 2009, **38**, 253–278.
8 T. W. Kim and K.-S. Choi, *Science*, 2014, **343**, 990–994.
9 S. J. A. Moniz, S. A. Shevlin, D. J. Martin, Z.-X. Guo and J. Tang, *Energy Environ. Sci.*, 2015, **8**, 731–759.
10 A. Kudo, K. Omori and H. Kato, *J. Am. Chem. Soc.*, 1999, **121**, 11459–11467.

11 S. Tokunaga, H. Kato and A. Kudo, *Chem. Mater.*, 2001, **13**, 4624–4628.
12 J. Q. Yu and A. Kudo, *Adv. Funct. Mater.*, 2006, **16**, 2163–2169.
13 F. Chen, H. Huang, L. Guo, Y. Zhang and T. Ma, *Angew. Chem., Int. Ed.*, 2019, **58**, 10061–10073.
14 H. Huang, S. Tu, C. Zeng, T. Zhang, A. H. Reshak and Y. Zhang, *Angew. Chem., Int. Ed.*, 2017, **56**, 11860–11864.
15 S. Obregón, S. W. Lee and G. Colón, *Dalton Trans.*, 2014, **43**, 311–316.
16 J. Jiang, L. Ou-yang, L. Zhu, A. Zheng, J. Zou, X. Yi and H. Tang, *Carbon*, 2014, **80**, 213–221.
17 Q. Xiang, J. Yu and M. Jaroniec, *J. Phys. Chem. C*, 2011, **115**, 7355–7363.
18 C.-Y. Chen, J. R. D. Retamal, I. W. Wu, D.-H. Lien, M.-W. Chen, Y. Ding, Y.-L. Chueh, C.-I. Wu and J.-H. He, *ACS Nano*, 2012, **6**, 9366–9372.
19 B. Pattengale and J. Huang, *Phys. Chem. Chem. Phys.*, 2017, **19**, 6831–6837.
20 H. Wang, X. Zhang, J. Xie, J. Zhang, P. Ma, B. Pan and Y. Xie, *Nanoscale*, 2015, **7**, 5152–5156.
21 H. Fan, T. Jiang, H. Li, D. Wang, L. Wang, J. Zhai, D. He, P. Wang and T. Xie, *J. Phys. Chem. C*, 2012, **116**, 2425–2430.
22 H. Kisch and D. Bahnemann, *J. Phys. Chem. Lett.*, 2015, **6**, 1907–1910.
23 S. Ho-Kimura, S. J. A. Moniz, A. D. Handoko and J. Tang, *J. Mater. Chem. A*, 2014, **2**, 3948–3953.
24 Y. Yuan, L. Zhang, J. Xing, M. I. B. Utama, X. Lu, K. Du, Y. Li, X. Hu, S. Wang, A. Genç, R. Dunin-Borkowski, J. Arbiol and Q. Xiong, *Nanoscale*, 2015, **7**, 12343–12350.
25 M. Ou, S. Wan, Q. Zhong, S. Zhang, Y. Song, L. Guo, W. Cai and Y. Xu, *Appl. Catal., B*, 2018, **221**, 97–107.
26 W. Yao and J. Ye, *J. Phys. Chem. B*, 2006, **110**, 11188–11195.
27 W. Yao and J. Ye, *Chem. Phys. Lett.*, 2008, **450**, 370–374.
28 Y. K. Kho, W. Y. Teoh, A. Iwase, L. Mädler, A. Kudo and R. Amal, *ACS Appl. Mater. Interfaces*, 2011, **3**, 1997–2004.
29 S. Usai, S. Obregón, A. I. Becerro and G. Colón, *J. Phys. Chem. C*, 2013, **117**, 24479–24484.
30 S. Obregón and G. Colón, *Appl. Catal., B*, 2014, **158–159**, 242–249.
31 S. Obregón and G. Colón, *Catal. Sci. Technol.*, 2014, **4**, 2042–2050.

